RSC Advances

PAPER

View Article Online
View Journal | View Issue

Cite this: *RSC Adv.*, 2023, **13**, 534

Crystal defect induced zero thermal quenching β-$NaYF_4$: Eu^{3+}, Sm^{3+} red-emitting phosphor

Shaokun Ling,[b] Xiaoyan Qin,[c] Yifeng Yan,[b] Chang Chen,[b] Kai Meng,[b] Junyun Ming,[b] Sen Liao, *[ab] Yingheng Huang*[b] and Lei Hou*[d]

Red phosphors with brilliant performance are crucial for the application of white LEDs as their red-light component. However, the thermal quenching phenomenon is an inevitable obstacle in the practical application of various types of red-light phosphors. In this study, we report the preparation of a novel type of phosphor, $NaYF_4$: 0.065Eu^{3+}, 0.002Sm^{3+}, possessing not only an energy transfer effect from Sm^{3+} to Eu^{3+} but also superior negative thermal quenching (NTQ) performance. The phosphor was synthesized *via* a one-step hydrothermal method, resulting in a prominent improvement in its luminous thermal stability supported by NTQ. The NTQ originated from the thermal stimulation excitement of the captured electrons in electronic traps, which is attributed to the non-equivalence between the different types of ions. The shape of the emission spectrum measured at high temperature was identical to that measured at room temperature, which not only showed the remarkable thermal stability of this novel type of phosphor but also the promising prospect of its practical application. This finding will contribute to improving the thermal stability of phosphor materials doped with lanthanide elements.

Received 18th October 2022
Accepted 25th November 2022

DOI: 10.1039/d2ra06567c

rsc.li/rsc-advances

1. Introduction

Light-emitting diodes (LEDs) provide a light source with the characteristics of low energy consumption and high luminous efficiency for various fields,[1] such as indoor illumination systems,[2] agricultural lighting for plants,[3] bedroom light in hospitals for comforting individuals,[4] and backlight source of mini-LED and micro-LED display systems.[5,6]

However, current commercial WLEDs still exhibit some problems that need to be solved, as follows: (a) they have a low color rendering index and high correlated color temperature caused by the traditional method for the combination of YAG: Ce^{3+} and InGaN chips with blue emission color[7,8] and (b) their emissions lack red-emitting phosphors.[9] Thus, to overcome these problems, researchers have devoted their attention to developing novel types of phosphors for application in WLEDs in recent years.[10–13] Remarkably, the thermal quenching effect of the YAG: Ce^{3+} phosphor,[14] which imposes deleterious influence on the luminous performance and lifetime, inevitably limits the performances of the current commercial WLEDs. Thus, red phosphors with outstanding thermal and chemical stability and luminous performance are urgently needed[2,15] to cooperate with the YAG: Ce^{3+} yellow phosphor.

Red-emitting phosphors of Eu^{2+}-doped nitride-based substrates have a broad red emission band and deep red color, such as $Sr[LiAl_3N_4]$: Eu^{2+},[16] $SrAlSi_4N_7$: Eu^{2+},[17] and $Ca_5Si_2Al_2N_8$: Eu^{2+}.[9] Noteworthily, $Sr[LiAl_3N_4]$: Eu^{2+} and $Ca_5Si_2Al_2N_8$: Eu^{2+} phosphors not only show deep red-light emission mainly centered at 650 nm, but also exhibit superior luminous thermal stability. In recent years, yellow and green emission nitride-based phosphors with zero thermal quenching property have been explored, for instance $Li_2CaSi_2N_4$: Ce^{3+} [18] and SiAlON: Eu^{2+}.[19] Researches proved that Eu^{2+}-doped nitride-based matrix phosphors with brilliant luminous thermal stability have good compatibility with different colors and great potential to be employed on a large scale. Unfortunately, despite their excellent luminous thermal stability and red-light emission performance, the rigorous conditions and high cost of their synthesis, which demand the maintenance of a high purity N_2 atmosphere for a long period at high temperature, restrain the practical production and application of nitride-based red-light emission phosphors.

Accordingly, due to the low phonon energy, narrow linewidth of emission band and brilliant chemical stability of fluoride-based phosphors, they have attracted significant attention from researchers and studied in distinct fields, such as LaF_3: RE^{3+} (RE^{3+} = Eu^{3+} and Tb^{3+}) layer in solar cells,[20] $NaErF_4$-based phosphor for anticounterfeiting,[21] $NaYF_4$-based nanoparticle for biological application,[22] and Cs_2SiF_6: Mn^{4+} in WLEDs.[23] Possessing the abundant merits of fluorides, $NaYF_4$ is an

[a]School of Chemistry and Chemical Engineering, Guangxi University, Nanning, Guangxi, 530004, China. E-mail: liaosen@gxu.edu.cn
[b]School of Resources, Environment and Materials, Guangxi University, Nanning, Guangxi, 530004, China. E-mail: huangyingheng@163.com
[c]School of Intelligent Equipment Engineering, Guangxi Agricultural Vocational and Technical University, 530009, China
[d]Publicity Department and United Front Work Department, Guangxi University of Information Engineering, 530200, China

outstanding matrix and exhibits high compatibility with lanthanides, for instance Eu, Yb, Er, Tm, Ho and Nd.[22,24] Furthermore, flexible routes can be employed for the synthesis of $NaYF_4$-based phosphors, such as thermal decomposition, hydrothermal method, electrospinning process, and microwave synthesis.[25–28] Among them, the hydrothermal method is the safest the most cost-effective for the synthesis of $NaYF_4$-based phosphors due to its convenient operation process and moderate synthesis environment, exhibiting high safety.[29]

The trivalent europium ion is an ideal red-light source due to its red photoluminescence.[30] This means that Eu^{3+} can be incorporated in the matrix as a fantastic activator of phosphors. Furthermore, to enhance the luminous intensity of Eu^{3+}, sensitizers must be considered. Owing to the existence of energy transfer from the $^4G_{5/2}$ of Sm^{3+} to $^5D_0$ of Eu^{3+},[31] the Sm^{3+} ion is an excellent sensitizer and can be co-doped in the matrix together with the Eu^{3+} ion.

In this study, utilizing $NaYF_4$ as the substrate and Eu^{3+} and Sm^{3+} as the activator and sensitizer, respectively, the hydrothermal method was employed to synthesize a novel type of β-$NaYF_4$: Eu^{3+}, Sm^{3+} red-light emission phosphor, which exhibited a outstanding red-light emitting performance and brilliant luminous stability at high temperature. This novel phosphor may not only provide a red-light source with excellent property for white-light emission diodes but also for the patterned color conversion layer[32] of mini-LED display technology.

2. Experiment

2.1 Experiment processes

In this work, a one-step hydrothermal method was utilized to synthesize a series of $NaYF_4$: $0.065Eu^{3+}$, xSm^{3+} phosphors ($x = 0$, 0.001, 0.002, 0.003, 0.004, and 0.005). In this study, $NaNO_3$, $Y(NO_3)_3 \cdot 6H_2O$, $Eu(NO_3)_3 \cdot 6H_2O$, and $Sm(NO_3)_3 \cdot 6H_2O$ were used as the raw materials. The synthesis process was as follows: (i) four types of solutions: $NaNO_3$ (2 mol L^{-1}), $Y(NO_3)_3$ (1 mol L^{-1}), $Eu(NO_3)_3$ (1 mol L^{-1}), and $Sm(NO_3)_3$ (1 mol L^{-1}) were blended according to the stoichiometric ratio of $1:1-(0.065+x):0.065:x$, named as solution A, and transferred to Teflon-lined containers. To achieve the homogeneous mixing of the solution, solution A was stirred for 20 min. (ii) Subsequently, 10 mL NH_4F (6 mol L^{-1}) solution was added to solution A and continually stirred for 30 min. (iii) The Teflon-lined stain-steel autoclaves containing the white precipitate were heated to 230 °C and kept for 72 h. (iii) The final products were washed several times using deionized water and anhydrous ethanol. (v) The products were washed and dried at the temperature of 120 °C for 3 h.

2.2 Characterization

The phase of the all samples was determined using a Bruke-D8 X-ray diffractometer with Cu target. Morphology observation and detection of the energy dispersive spectra of the samples were performed using a high-resolution scanning electron microscope (Hitachi SU8020, Japan). XPS spectra were measured using an ESCALAB 25XI. A JEM-2100F was employed to obtain the high-resolution transmission electron microscopy (HRTEM) and selected area electron diffraction (SAED) images. A HORIBO FluoroMax4 spectrophotometer was employed to measure the fluorescence spectra and lifetime of the phosphors at room and high temperature. Finally, electron paramagnetic resonance (EPR) on a Bruker model was utilized to characterize the crystal defects.

3. Result and discussion

3.1 Crystal structure and element characterization

As illustrated in Fig. 1a, the positions of the diffraction peaks of all the samples are consistent with that of the standard card, PDF#-281179, $Na(0.57Y0.39Yb0.04Er)F_4$, in the 2θ range of 10° to 90°. Compared with the standard PDF card, the diffraction peak positions slightly shifted to a lower degree in the range of 92° to 120°, as shown in Fig. 1b. This result is caused by the larger ion radius of Y^{3+}, which is larger than that of Yb^{3+} and Er^{3+}. This result led to an enlargement in the crystal face distance. Besides, compared with the XRD pattern of $NaYF_4$: $0.065Eu^{3+}$, the 2θ value of $NaYF_4$: $0.065Eu^{3+}$, xSm^{3+} also present

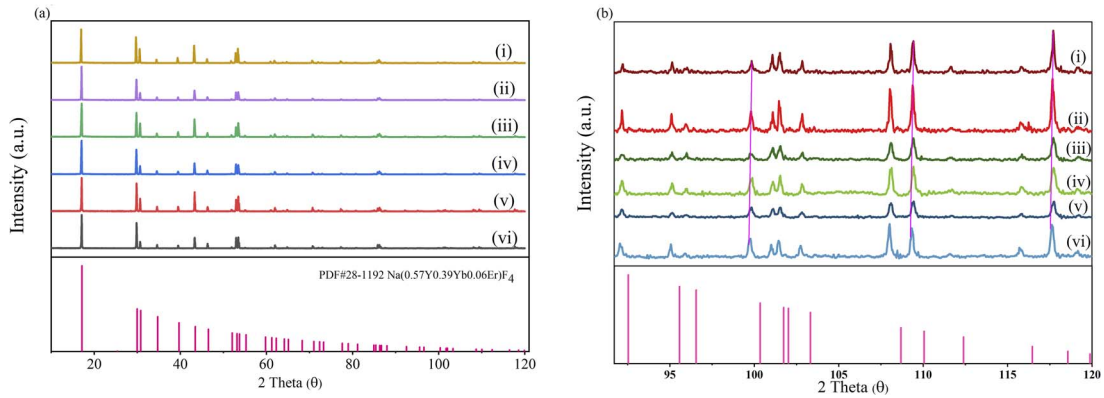

Fig. 1 (a) XRD patterns of (i)$NaYF_4$: $0.065Eu^{3+}$. (ii) $NaYF_4$: $0.065Eu^{3+}$, $0.001Sm^{3+}$. (iii) $NaYF_4$: $0.065Eu^{3+}$, $0.002Sm^{3+}$. (iv)$NaYF_4$: $0.065Eu^{3+}$, $0.003Sm^{3+}$. (v) $NaYF_4$: $0.065Eu^{3+}$, $0.004Sm^{3+}$. (iv) $NaYF_4$: $0.065Eu^{3+}$, $0.005Sm^{3+}$. (b) XRD patterns of all $NaYF_4$: $0.065Eu^{3+}$, xSm^{3+} ($x = 0-0.005$) samples in the range of 92° to 120°.

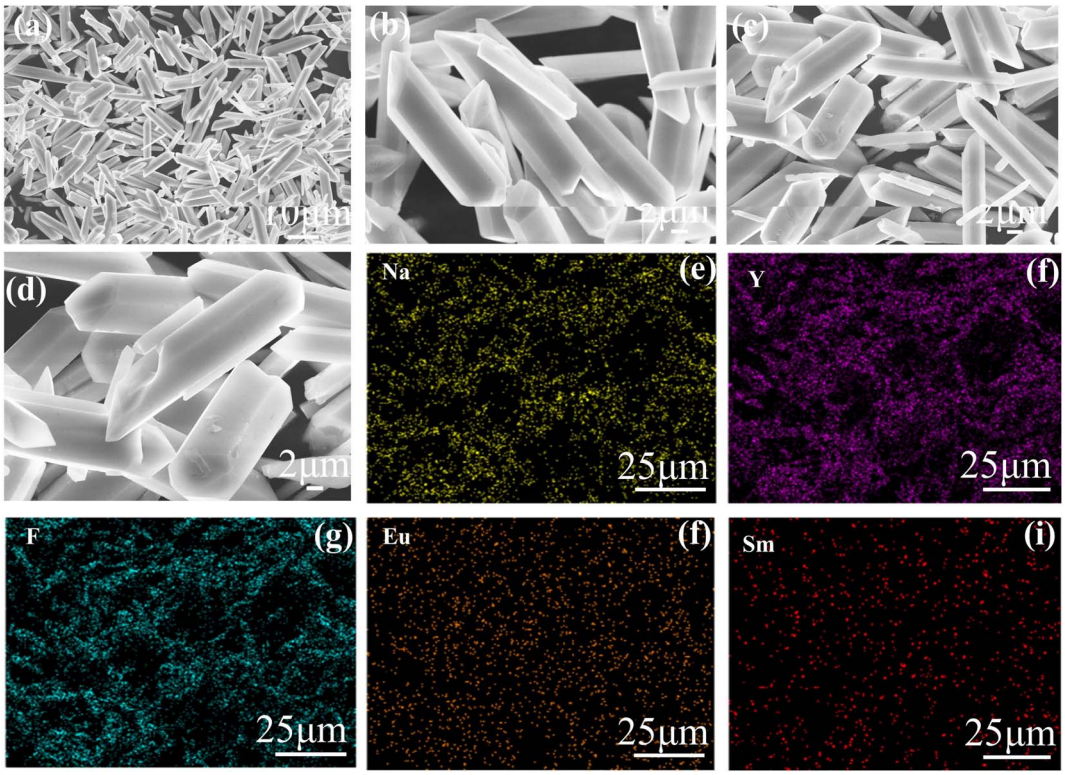

Fig. 2 Crystalline grain morphology of $NaYF_4$: $0.065Eu^{3+}$, $0.002Sm^{3+}$ at a magnification of (a) 1.0 K, (b) 3.0 K, (c) 4.0 K and (d) 5.0 K. Energy dispersive spectroscopy mapping patterns of (e) Na, (f) Y, (g) F, (h) Eu and (i) Sm elements.

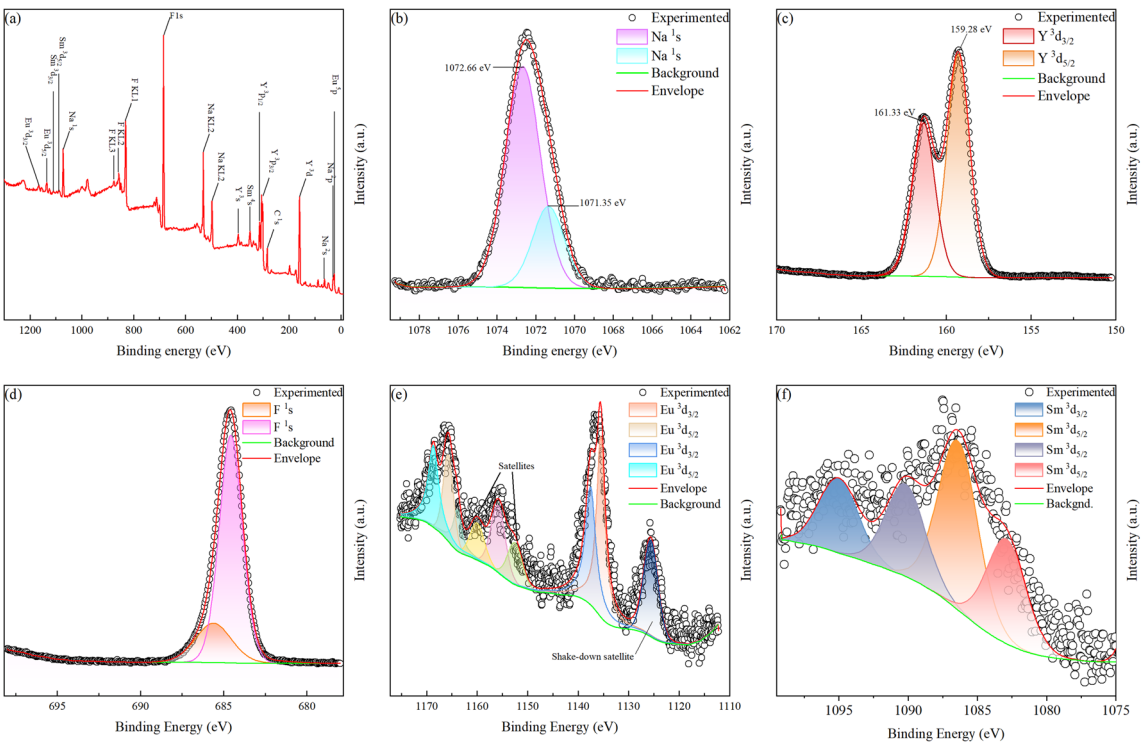

Fig. 3 XPS spectra of $NaYF_4$: $0.065Eu^{3+}$, $0.002Sm^{3+}$ composite (a) survey of sample. High-resolution spectra of (b) Na 1s, (c) Y 3d, (d) F 1s, (e)Eu 3d, and (f) Sm 3d.

a minor shift from high to low angle with an increase of the concentration of Sm^{3+}, which was caused by the decrease of the crystal face distance induced by the increasing concentration of incorporated Sm^{3+} ion. Notably, impurity phases were absent in all the XRD patterns of the samples.

The crystalline grain morphology, as shown in Fig. 2a–d, was observed by scanning electron microscopy at the magnification of 1.0 K, 3.0 K, 4.0 K, and 5.0 K, respectively. According to the depictions, the crystal grain of $NaYF_4$: $0.065Eu^{3+}$, $0.002Sm^{3+}$ belongs to a dendritic crystal with a thin and long shape. The length and diameter of the dendritic crystal is approximately 10 μm and 4 μm, respectively. Meanwhile, energy dispersive spectroscopy (EDS) was implemented simultaneously to confirm the elements present in the samples. The EDS mapping result is shown in Fig. 2e–i. The element mapping patterns clearly demonstrate that the Na, Y, F, Eu, and Sm elements were uniformly distributed in the crystal grain.

Fig. 3a shows the full survey XPS spectra and refined element spectra of $NaYF_4$: $0.065Eu^{3+}$, $0.002Sm^{3+}$. Fig. 3a further certifies that Eu^{3+} and Sm^{3+} ions were successfully incorporated in the $NaFY_4$ matrix. Notably, Sm 4s shows an evident peak in the full survey XPS spectrum. Besides, KL1, KL2, and KL3 of Na and KL1 and KL2 of F are attributed to the Auger kinetic energy of the elements. Fig. 3b–d will be further analyzed in Section 3.3. Fig. 3e exhibits the XPS spectra of Eu. In the binding energy range of 1148.35 eV to 1162.20 eV, other satellites[33] peaks were detected. Besides, the shake-down satellite[33] was measured in the range of 1125.63 eV to 1137.55 eV. Double separation of $3d_{5/2}$ existed in the binding energy range of 1165.72 eV to 1168.69 eV. As shown in Fig. 3f, the XPS spectrum of Sm illustrates that a series of separation peaks located at 1096.99 eV can be attributed to Sm $^3d_{3/2}$. At the binding energies of 1090.25 eV, 1086.50 eV and 1083.05 eV, the separation peaks are ascribed to the Sm $^3d_{5/2}$ energy level.

The morphology of the crystal grain was investigated by transmission electron microscopy, as presented in Fig. 4a. The high-resolution transmission electron microscopy image is presented in Fig. 4b, showing the crystal face distance of [100] and [110] corresponding to 0.5341 nm and 0.282 nm, respectively. The selected area electron diffraction image is illustrated in Fig. 4c. As presented, the central diffraction spot represents the [100] face. Besides, the other marked diffraction spot corresponds to the [110] face. According to Fig. 4c, a redundant spot referring to an impurity phase was not detected. This result is well consistent with the XRD patterns depicted in Fig. 1a and b. To accurately acquire the crystal cell volume and crystal structure information, refinement of X-ray diffraction was implemented through the GSAS program. The refinement result of the X-ray diffraction data is illustrated in Fig. 4d. The R_{wp}, R_p and χ^2 of the refined data are 8.47%, 6.49% and 2.144, respectively, which indicate the high quality and reliable result of the fit. The Sm^{3+} ion was not considered in the refinement due to its low content, barely contributing to the X-ray diffraction. The crystal structure information is listed in Table 1, indicating that the space group of $NaYF_4$: $0.065Eu^{3+}$, $0.002Sm^{3+}$ with the cell volume of 109.212 Å belongs to $P63/m$ (176).

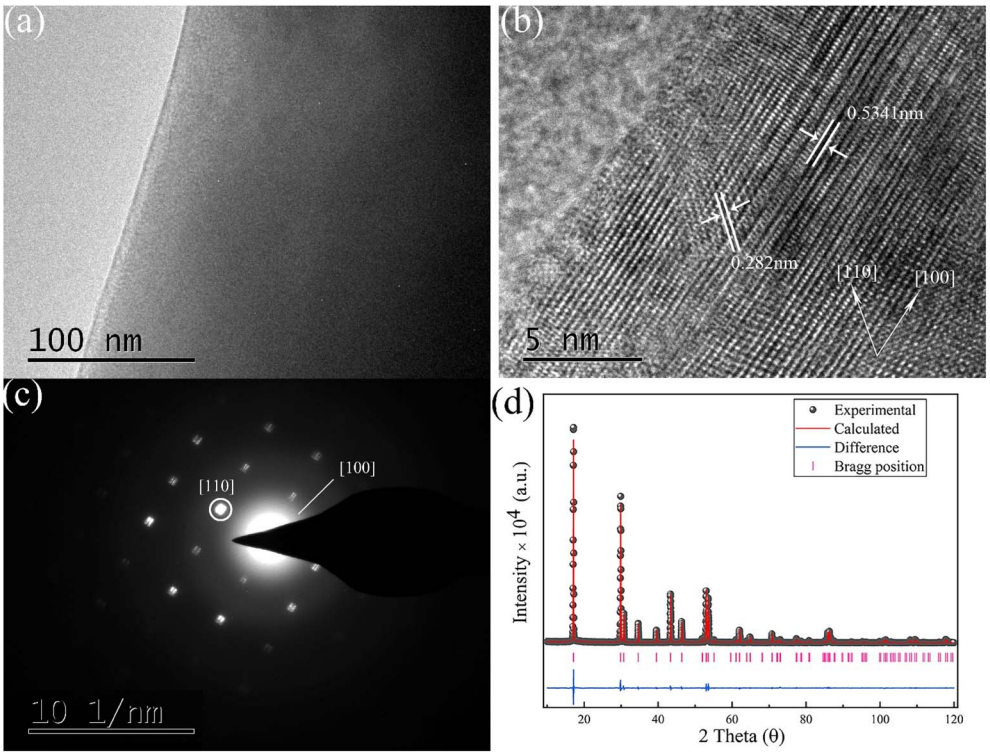

Fig. 4 (a) Margin region of grain of $NaYF_4$: $0.065Eu^{3+}$, $0.002Sm^{3+}$ detected by TEM. (b). HRTEM of $NaYF_4$: $0.065Eu^{3+}$, $0.002Sm^{3+}$. (c) SAED graph of the sample. (d) Refined XRD pattern of $NaYF_4$: $0.065Eu^{3+}$, $0.002Sm^{3+}$.

Table 1 The Rietveld refinement results of β-$NaYF_4$: 0.065Eu^{3+}

Formula sum	β-$NaYF_4$: 0.065Eu^{3+}			
Formula weight	197.7661			
Crystal system	Hexagonal			
Space group	*P*63/*m*			
Cell parameters	a = 5.984911 (28)Å	b = 5.984911 Å	c = 3.5206(5) Å	
Cell volume	109.212(20)			
Z	6			
Atom	x/a	y/b^1	z/c	Occupation
Na1	0.0	0.0	0.11747 (22)	0.71
Na2	0.6667	0.3333	0.25	0.18
Y1	0.6667	0.3333	0.25	0.755
Y2	0.0	0.0	0.11747 (22)	0.29
Eu1	0.6667	0.3333	0.25	0.065
F1	0.2933(5)	0.3165 (4)	0.25	1.0

Base on the refined result, the crystal structure graph, as presented in Fig. 5, was drawn using the diamond 3 program. According to Fig. 5a, the structure can be observed from the parallel perspective to the connection of the vertex of the a and c axes, where Y–F decahedron and Na–F octahedron constitute an integrated crystal cell. Fig. 5b and c display the Y–F decahedron observed along the a-axis direction and Na–F octahedron along the c-axis, respectively. Notably, the Na–F octahedron, named as $[Na_2F_6]$, is composed of two central Na atoms and six ligand F atoms. In the cell edge parallel to the connection of the vertex of

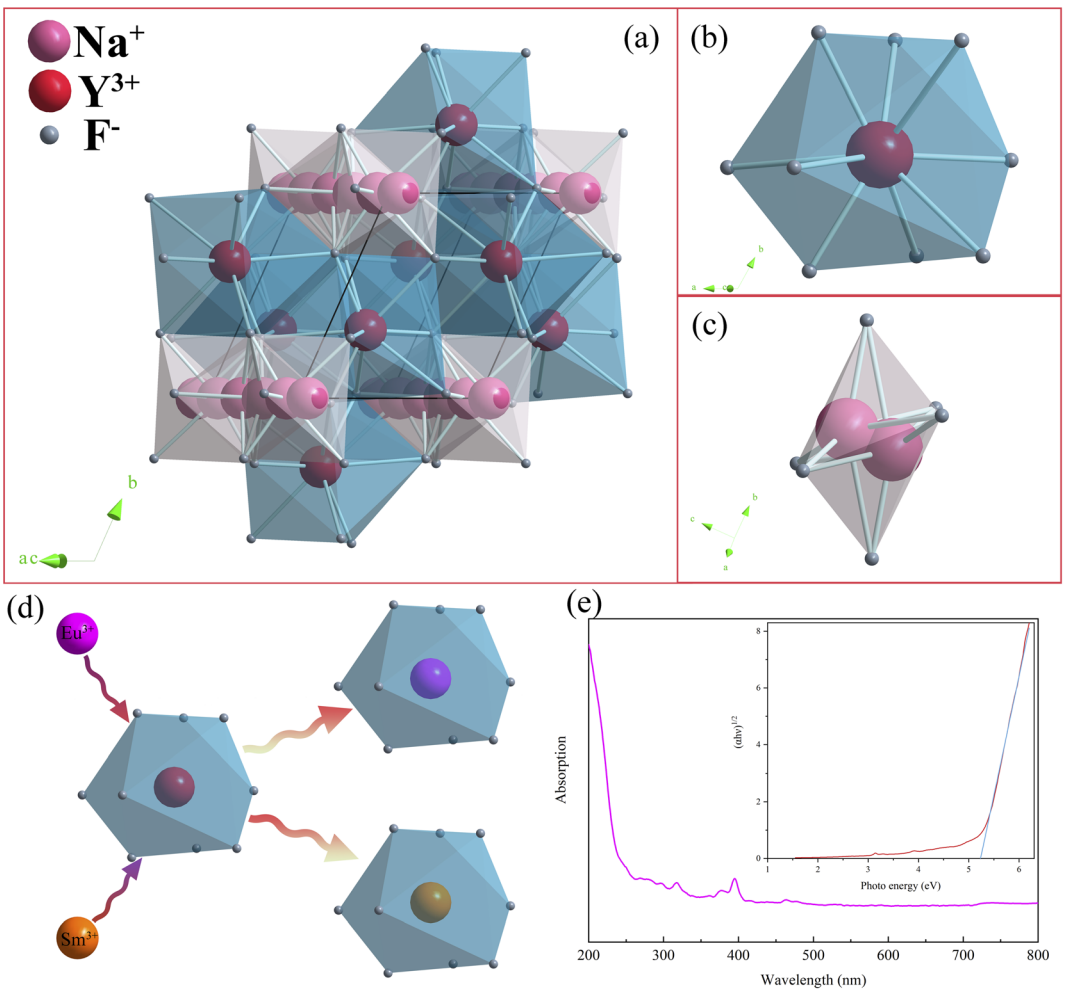

Fig. 5 (a) Crystal structure of β-$NaYF_4$. (b) Y–F decahedron. (c) Na–F octahedron. (d) Mechanism of the incorporation of Eu^{3+} and Sm^{3+} ions. (e) Ultraviolet visible absorption spectrum of $NaYF_4$: 0.065Eu^{3+}, 0.002Sm^{3+}.

a and *c* axis direction, three $[Na_2F_6]$ octahedrons are connected with each other through F atoms. There is one Y atom and nine F atoms, as the central atom and ligand atoms, respectively, constituting the Y–F decahedron, named as the $[YF_9]$ decahedron. Based on the XPS and EDS results, Eu^{3+} and Sm^{3+} ions were incorporated in the $[YF_9]$ decahedron. The incorporation mechanism is presented in Fig. 5d.

The energy gap of $NaYF_4$: $0.065Eu^{3+}$, $0.002Sm^{3+}$ was calculated according to the ultraviolet visible absorption spectra and shown in Fig. 5e using following equation:[34]

$$(\alpha h\nu)^n = A(h\nu - E_g) \quad (1)$$

where A, α, ν, and h represent a constant, absorption coefficient, frequency, and Planck's constant, respectively. E_g represents the energy gap and n is equal to 2 or 1/2. When n is equal to 2, the calculated result indicates a direct energy gap, whereas if n is 1/2, the calculated result from the UV-vis spectra indicates an indirect energy gap. In this study, employing $n = 1/2$ to calculate the direct energy gap, the calculated energy gap (E_g) is equal to 5.33 eV. This large energy gap provides a suitable environment for the coordination of the Eu^{3+} and Sm^{3+} ions in the β-$NaYF_4$ substrate.

3.2 Luminescence property of β-$NaYF_4$: $0.065Eu^{3+}$, xSm^{3+} (x = 0, 0.001, 0.002, 0.003, 0.004, and 0.005)

The emission spectra of the series $NaYF_4$: $0.065Eu^{3+}$, xSm^{3+} phosphors were measured at room temperature (RT). Under the emission of 393 nm, Fig. 6a illustrates the emission spectra of all the samples doped with different concentrations of Sm^{3+} in the range of 0 to 0.005 mol. The main emission peaks are located at 616 nm for all the samples. Based on the Judd–Ofelt theory,[35,36] the transition intensity ratio of $^5D_0 \rightarrow {}^7F_2$ to $^5D_0 \rightarrow {}^7F_1$ ($R = I_2/I_1$) of Eu^{3+} is a critical criterion to determine the emission mode dominated by the magnetic dipole (MD) transition ($^5D_0 \rightarrow {}^7F_1$) or the electric dipole (ED) transition ($^5D_0 \rightarrow {}^7F_2$). If $R > 1$, it means that the emission is dominated by the ED transition and corresponds to a red light. On the contrary, when $R < 1$, it is results from an emission dominated by the MD transition and corresponds to a reddish-orange light. Upon excitation at 393 nm, the value of R was calculated to be 1.68, which suggests that the emission of $NaYF_4$: $0.065Eu^{3+}$, $0.002Sm^{3+}$ is determined by the ED transition. The orange-red light of the samples originate from the increasing emission intensity of $^5D_0 \rightarrow {}^7F_2$, which is induced by the Eu^{3+} ion in the inversion symmetry center.[37] It can be seen from Fig. 6b that the luminous intensities of the samples co-doped with Sm^{3+} ion are much higher than that of the sample without co-doped Sm^{3+} ion. The luminous intensity of $NaYF_4$: 0,$065Eu^{3+}$, $0.002Sm^{3+}$ is 128.89%, 197.19%, 174.53%, 138.11%, and 139.69% that of $NaYF_4$: $0.065Eu^{3+}$, which suggests the existence of an enhancement effect induced by Sm^{3+}. However, when the concentration of Sm^{3+} was greater than 0.002, the luminescence intensity gradually decreased, which refers to concentration quenching (CQ) phenomenon. To elucidate the mechanism of CQ, the following equation[38] was applied:

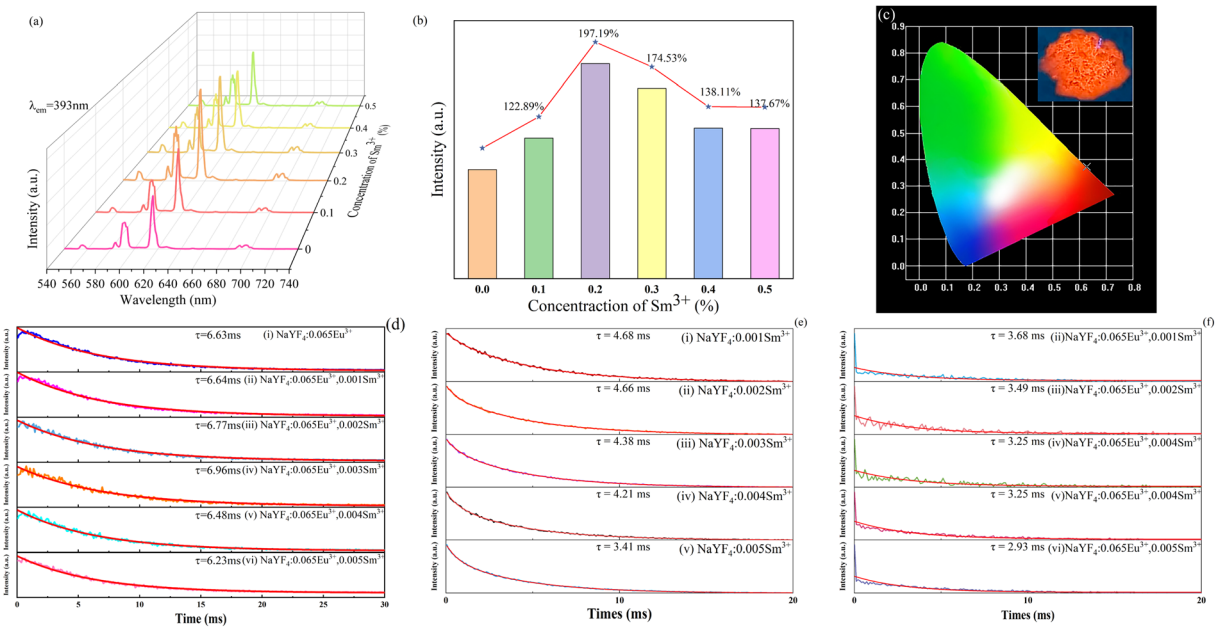

Fig. 6 (a) Emission spectra of the samples doped with different concentrations of Sm^{3+}. (b) Intensity of the major emission peak when the doping concentration is in the range of 0 to 0.005. (c) CIE chromaticity diagram and luminous photo of $NaYF_4$: $0.065Eu^{3+}$, $0.002Sm^{3+}$. (d) Room temperature decay of Eu^{3+} ion of (i) $NaYF_4$: $0.065Eu^{3+}$. (ii) $NaYF_4$: $0.065Eu^{3+}$, $0.001Sm^{3+}$. (iii) $NaYF_4$: $0.065Eu^{3+}$, $0.002Sm^{3+}$. (iv) $NaYF_4$: $0.065Eu^{3+}$, $0.003Sm^{3+}$. (v) $NaYF_4$: $0.065Eu^{3+}$, $0.004Sm^{3+}$. (vi) $NaYF_4$: $0.065Eu^{3+}$, $0.005Sm^{3+}$. (e) Room temperature decay of Sm^{3+} ion of (i) $NaYF_4$: $0.001Sm^{3+}$, (ii) $NaYF_4$: $0.002Sm^{3+}$, (iii) $NaYF_4$: $0.003Sm^{3+}$, (iv) $NaYF_4$: $0.004Sm^{3+}$, and (v) $NaYF_4$: $0.005Sm^{3+}$. (f) Room temperature decay of Sm^{3+} ion of (ii) $NaYF_4$: $0.065Eu^{3+}$, $0.001Sm^{3+}$, (iii) $NaYF_4$: $0.065Eu^{3+}$, $0.002Sm^{3+}$, (iv) $NaYF_4$: $0.065Eu^{3+}$, $0.003Sm^{3+}$, (v) $NaYF_4$: $0.065Eu^{3+}$, $0.004Sm^{3+}$, and (vi) $NaYF_4$: $0.065Eu^{3+}$, $0.005Sm^{3+}$.

$$R_c = 2\sqrt[3]{\frac{3V}{4\pi x_c N}} \quad (2)$$

where V, x_c, and N is equal the crystal cell volume, concentration of sample corresponding to the optimal luminescence intensity, and number of possible replacement sites of Eu^{3+} and Sm^{3+}, respectively. In this work, V, x_c, and N correspond to 109.212 Å, 0.067, and 8, respectively. The R_c value was calculated to be 7.300 Å, which is much higher than 5 Å. The calculated result of R_c also suggests that the electric multipolar interaction is a dominant factor in the concentration quenching.[38]

As demonstrated in Fig. 6d, the decay lifetime of Sm^{3+} with a concentration in the range of 0 to 0.005 was measured at room temperature (RT). The decay lifetime was calculated using eqn (3).[39]

$$I_t = A_1\exp\left(-\frac{t}{\tau_1}\right) + A_2\exp\left(-\frac{t}{\tau_2}\right) + I_0 \quad (3)$$

where I_t and I_0 are the luminescence intensity at selected time t and 0, respectively. A_1 and A_2 are constants and τ_1 and τ_2 are the rapid and slow time decay constants, respectively. According to eqn (3), the average decay lifetime is expressed as the following expression:

$$\tau = \left(A_1\tau_1^2 + A_2\tau_2^2\right)/\left(A_1\tau_1 + A_2\tau_2\right) \quad (4)$$

The calculated and fitted results show that the decay lifetime was prolonged from 6.63 ms to 6.96 ms when the concentration of Sm^{3+} was increased from 0 to 0.003, which suggests the occurrence of energy transfer from the Sm^{3+} to Eu^{3+} ion.[40,41] A reduction in the decay lifetime from 6.48 ms to 6.23 ms was detected when the concentration of Sm^{3+} is higher than 0.004.

To further confirm that the energy transfer occurred from the Sm^{3+} to Eu^{3+} ion, the decay of Sm^{3+} without and with Eu^{3+} was measured, as shown in Fig. 6e and f, respectively. The decay lifetime of the Sm^{3+} of $NaYF_4$: xSm^{3+} samples decreased by 1.0 ms, 1.17 ms, 1.13 ms, 0.96 ms, and 0.48 ms compared with that of Sm^{3+} of the $NaYF_4$: $0.065Eu^{3+}$, xSm^{3+} samples, also indicating existence of energy transfer from Sm^{3+} to Eu^{3+}. Although a relatively longer decay time was observed for $NaYF_4$: $0.065Eu^{3+}$, $0.003Sm^{3+}$ than $NaYF_4$: $0.065Eu^{3+}$, $0.002Sm^{3+}$, the changes in the luminous intensity and decay lifetime indicate that concentration quenching is the predominant factor when the concentration of Sm^{3+} is over 0.003. The energy transfer efficiency was calculated according to the following equation:[38]

$$\eta = \frac{I_S - I_0}{I_0} \quad (5)$$

where I_s and I_0 represent the emission intensity of Sm^{3+} in the presence and absence of Eu^{3+}. When the concentration of Sm^{3+} increased from 0.001 to 0.002, the energy transfer efficiency of Sm^{3+} to Eu^{3+} sharply increased from 12.54% to 43.44%. When the concentration of Sm^{3+} was 0.003, 0.004, and 0.005, the energy transfer efficiency was calculated to be 35.46%, 33.62%, and 22.81%, respectively. The decline in energy transfer efficiency can be attributed to the non-radiative transition process. The trend of energy transfer efficiency is identical to the change in fluorescence intensity.

To elucidate the enhancement mechanism of Sm^{3+} to Eu^{3+}, the following relationship equation is employed to make a clear expression:[42]

$$I/x = k\,[1 + \beta(x)^{\theta/3}]^{-1} \quad (6)$$

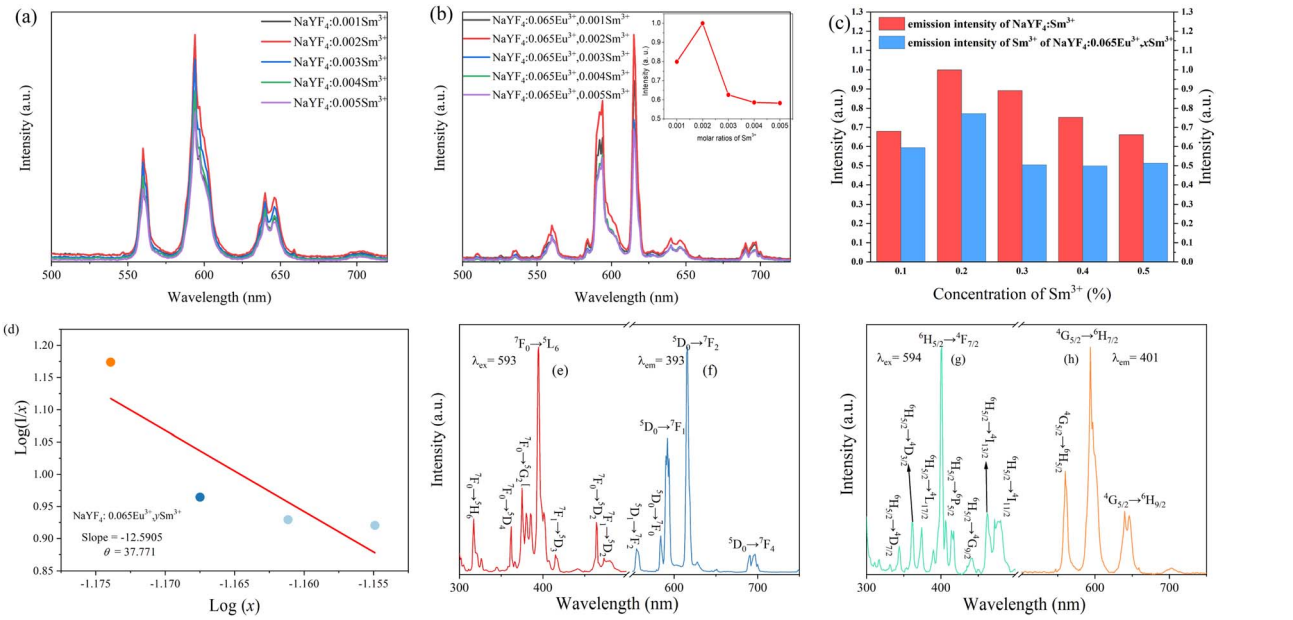

Fig. 7 (a) Emission spectra of $NaYF_4$: xSm^{3+}. (b) Emission spectra of samples with Sm^{3+} and Eu^{3+}. (c) Value of major emission peak of Sm^{3+} with and without Eu^{3+} ion. (d) Relationship between log (x) and log (I/x). (e) Excitation spectrum Eu^{3+} of $NaYF_4$: $0.065Eu^{3+}$, $0.002Sm^{3+}$. (f) Emission spectrum of Eu^{3+} of $NaYF_4$: $0.065Eu^{3+}$, $0.002Sm^{3+}$. (g) Emission spectrum of $NaYF_4$: $0.002Sm^{3+}$. (h) Excitation spectrum of $NaYF_4$: $0.002Sm^{3+}$.

In this equation, I represents the fluorescence intensity of Eu^{3+}. x is equal to the total concentration of Eu^{3+} and Sm^{3+} ions, where the concentration of Sm^{3+} is in the range of 0.002 to 0.005. The value of β can be 6,8, and 10, which represent the dipole–dipole, the dipole–quadrupole and the quadrupole–quadrupole interactions, respectively. k and β are constants for the same excitation condition. To obtain the luminous intensity, the emission spectra of Sm^{3+} of the $NaYF_4$: xSm^{3+} (spectra I) and $NaYF_4$: $0.065Eu^{3+}$, xSm^{3+} (spectra II) samples were measured under excitation at 401 nm, as shown in Fig. 7a and b, respectively. The intensities of the major emission peak for spectra I and II are presented in Fig. 7c for convenient observation and further discussion of the energy transfer mechanism. Notably, the emission peaks present at 616 nm and 675 nm to 700 nm can be ascribed to the emission of the Eu^{3+} ion, as illustrated in Fig. 7b. As shown in Fig. 7d, according to the linear fitness, the slope of the line is −12.5909. The value of θ was calculated to be 37.771, which is larger than 10. This result indicates that the energy transfer mechanism from Sm^{3+} to Eu^{3+} is the quadrupole–quadrupole interaction. To clearly describe the transition of electrons and energy transfer process, the emission and excitation spectra of Eu^{3+} in $NaYF_4$: $0.065Eu^{3+}$, $0.002Sm^{3+}$ and $NaYF_4$: $0.002Sm^{3+}$ were measured, as shown in Fig. 7e–h.

To elucidate the energy transfer from Sm^{3+} to Eu^{3+}, the excitation spectrum of $NaYF_4$: $0.065Eu^{3+}$ and emission spectrum of $NaYF_4$: $0.002Sm^{3+}$ are shown in Fig. 8a and b, respectively. Combining Fig. 7e–h with Fig. 8a and b, a schematic diagram of the energy transfer from Sm^{3+} to Eu^{3+} is shown in Fig. 8c. Under the emission of 393 nm, there are five major emission peaks, emerging at the positions of 616 nm, 592 nm, and 555 nm, which can be attributed to the transitions of $^5D_0 \rightarrow {}^7F_2$, $^5D_0 \rightarrow {}^7F_1$, and $^5D_1 \rightarrow {}^7F_2$ of Eu^{3+}, respectively. Comparing 393 nm with 401 nm, due to the higher energy of 393 nm, it allows Sm^{3+} to be excited from the ground state to the excited state. Under excitation of 393 nm, there are three main peaks in the emission spectrum, appearing at the positions of 560 nm, 594 nm, and 640 nm, which are attributed to the transitions of the $^4G_{5/2} \rightarrow {}^6H_{5/2}$, $^4G_{5/2} \rightarrow {}^6H_{7/2}$, and $^4G_{5/2} \rightarrow {}^6H_{9/2}$ energy level of Sm^{3+}, respectively. Notably, energy transfer occurs from $^4G_{5/2}$ to $^5D_0$, which results from the luminous enhancement of Eu^{3+}, while the transition of $^4G_{5/2} \rightarrow {}^6H_{K/2}$ ($K = 5, 7, 9$) occurs.

3.3 Thermal luminescence property

The thermal luminous property of $NaYF_4$: $0.065Eu^{3+}$, $0.002Sm^{3+}$ was characterized by emission spectra measured in the temperature range of 303 K to 543 K, under emission of 393 nm, as portrayed at Fig. 9a. Notably, no new emission peak emerged in all the emission spectra. The emission spectra measured at high temperature are consistent with the emission spectra at room temperature. The integrated luminous intensity of $NaYF_4$: $0.065Eu^{3+}$, $0.002Sm^{3+}$ at different temperatures is depicted in Fig. 9b. It can be seen that the intensity gradually enhanced with an increase in temperature in the range of 303 K to 483 K, showing that the luminous intensity at 483 K is 229.82% of that at 303 K. After 483 K, the luminescence intensity started to decline steadily from 483 K to 543 K. Although a lower luminous intensity was detected at 543 K than that at 483 K, the luminous intensity of the sample at 543 K was still 184.20% of that at 303 K. This result evidently displays that $NaYF_4$: $0.065Eu^{3+}$, $0.002Sm^{3+}$ possesses brilliant thermal luminescence stability with an increase in temperature, which is known as negative thermal quenching (NTQ), causing it to exhibit brilliant thermal luminous stability. Fig. 9c demonstrates the CIE color coordinates of $NaYF_4$: $0.065Eu^{3+}$, $0.002Sm^{3+}$. Fig. 9c shows a negligible shift in the red light region with an increase in temperature, suggesting that the sample has superior red emitting stability at high temperature. Fig. 9d illustrates the decay curves of $NaYF_4$: $0.065Eu^{3+}$, $0.002Sm^{3+}$ in the temperature range of 303 K to 543 K. Remarkably, the fitted results manifest that the decay lifetime increased from 6.87 ms at 303 K to 7.05 ms at 363 K. Due to the energy transfer effect, the electrons captured in the traps would be excited to the excited state with the help of the increasing thermal energy with the increase in temperature, prolonging the decay of the phosphor.[38] Other reports[43,44] also showed that this crystal exhibited abnormal thermal quenching. The effect of energy transfer from the traps to electrons is superior to the non-radiative transition in this stage.

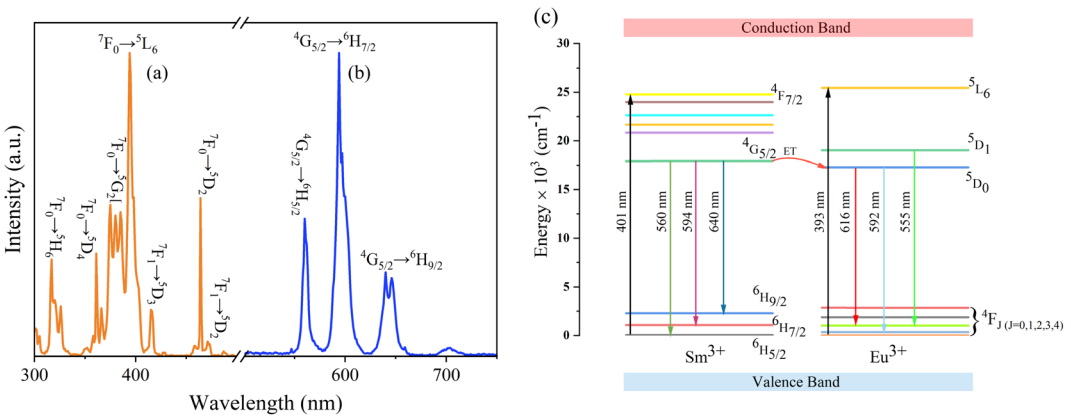

Fig. 8 (a) Excitation spectra of $NaYF_4$: $0.065Eu^{3+}$. (b) Emission spectra of $NaYF_4$: $0.002Sm^{3+}$. (c) Energy level and electric transition schematic diagram of Sm^{3+} and Eu^{3+}.

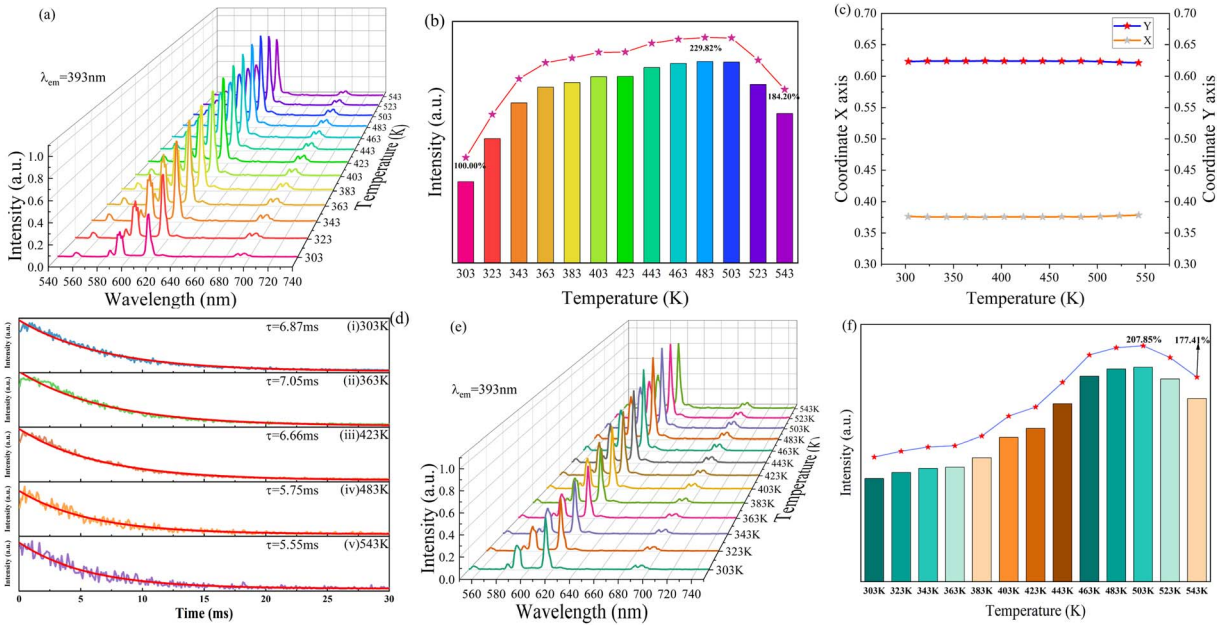

Fig. 9 (a) Emission spectrum of $NaYF_4$: $0.065Eu^{3+}$, $0.002Sm^{3+}$ at a distinct temperature. (b) Luminous intensity of the primary emission peak of $NaYF_4$: $0.065Eu^{3+}$, $0.002Sm^{3+}$ in the temperature range of 303 K to 543 K. (c) Change of CIE color coordinates. (d) Decay of $NaYF_4$: $0.065Eu^{3+}$, $0.002Sm^{3+}$ at (i) 303 K, (ii) 363 K, (iii) 423 K, (vi) 483 K, and (v) 543 K. (e) Emission spectrum of $NaYF_4$: $0.065Eu^{3+}$ at a distinct temperature. (f) Luminous intensity of primary emission peak of $NaYF_4$: $0.065Eu^{3+}$ at temperature 303 K to 543 K.

Meanwhile, the decay showed a continuous decline from 6.66 ms at 423 K to 5.55 ms at 543 K, which is attributed to the boosted probability of non-radiative transition induced by the increase in thermal energy.[45,46] Alternatively, the non-radiative transition probability gradually increased from 423 K and became the predominant effect rather the energy transfer effect after heating to 543 K. This process corresponds to the reduction of the number of electrons in the traps in temperature range from 423 K to 543 K compared with a temperature lower than 423 K. The emissions spectra of $NaYF_4 0.065Eu^{3+}$ and the major peak value in the temperature range of 303 K to 543 K are illustrated in Fig. 9e and f, respectively. The $NaYF_4 0.065Eu^{3+}$ sample showed an outstanding thermal luminous performance. This result shows that the incorporation of Sm^{3+} had no influence on the thermal property of $NaYF_4$: $0.065Eu^{3+}$, $0.002Sm^{3+}$, it only acted as a sensitizer to enhance the luminous property of Eu^{3+}.

3.4 Mechanism of negative thermal quenching

To elucidate the mechanism of NTQ, the crystal defect formed from the inequivalence replacement of the ions should be considered. According to the information in Table 1, the Y^{3+} ion was incorporated in the position of Na1 ($x = 0.0$, $y = 0.0$, $z = 0.11747$), which is defined as the Y2 site. Similarly, the Y^{3+} ion in the site x, y, and z of 0.6667, 0.3333, 0.25, respectively, is defined as Y1. The Na^+ ion that occupies this position is named Na2. This result suggests the replacement of Na^+ ($CN = 6$, $R = 1.02$ Å) with the Y^{3+} ($CN = 9$, $R = 1.075$ Å) ion. The process of inequivalence replacement can be inferred and expressed using the following expression:

$$Y^{3+} + Na^+ \rightarrow V''_{Na} + V^{\cdot\cdot}_{Na} \quad (7)$$

$$Na^+ + Y^{3+} \rightarrow V''_{Y} + V^{\cdot\cdot}_{Y} \quad (8)$$

Eqn (7) indicates that the incorporation of Y^{3+} in the Na1 site produces two anionic vacancies $V^{\cdot\cdot}_{Na}$ and cation defect V''_{Na} to balance the electroneutrality. Analogously, in eqn (7), when an Na^+ ion is incorporated in the Y1 site, there are two vacancies with positive charge ($V^{\cdot\cdot}_{Y}$) and two defects with negative charge (V''_{Y}) to maintain the balance of electroneutrality induced by nonequivalent replacement. These crystal defects act as electronic traps to store and release electrons.[38,47,48] As confirmed by the XPS refined spectra of Y^{3+} and Na^+, the chemical bonds changed during the nonequivalent replacement. The high-resolution spectra of Na^+, as illustrated in Fig. 3b, indicate two types of binding energies of 1071.35 eV and 1072.66 eV, which are close to the Na–F binding energies of 1071.30 eV[49] and 1072.70 eV.[50] This result indicates the existence of two types of Na–F bonds, resulting from the nonequivalent replacement. Some of the $[Na_2F_6]$ octahedrons would shift to $[NaYF_6]$ octahedrons. Similarly, according to the high-resolution spectra of Y^{3+} presented in Fig. 3c, there are two types of peaks located at the binding energies of 159.28 eV and 161.33 eV, which are close to 159.10 eV[51] and 161.20 eV.[52] This binging energy also demonstrates the existence of two different bonds of Y–F induced by the replacement between Y^{3+} and Na^+. Some of the $[YF_9]$ decahedrons would transfer to $[NaF_9]$ decahedrons. As shown in Fig. 3d, the XPS spectra of F indicate two types of binding energies, which demonstrate the existence of Na–F and Y–F bonds.

As is well known, electron paramagnetic resonance (EPR) is a suitable method to characterize solid defects. In this study, EPR was employed to provide powerful proof of the existence of defects. The EPR results are depicted in Fig. 10b, which show an asymmetric EPR signal. The EPR signal was detected in the magnetic field range of 2790 *G* to 4136 *G* and presented an evident attenuation with an increase in the measurement temperature. This signal indicates the existence of crystal defects. Based on the EPR result, the *g* value, a critical parameter for crystal defects, was calculated using the following equation:[53]

$$g = \frac{h\nu}{\beta B_0} \tag{9}$$

where ν represents the measurement frequency. B_0 is equal to the intensity of the magnetic field. h and β are Planck's constant and Bohr magneton, respectively. As illustrated in Fig. 10c, the *g* value based on the EPR result measured at 100 K, 200 K, and 298 K was calculated to be 1.977, 1.979, and 1.998, confirming the existence of crystal defects. A previous report on the EPR of K_2SiF_6: Mn^{4+} indicated that the *g* value of the sample is 1.8–2.2, providing valid proof for the existence of defects.[54] Another report employed EPR to detect the defects in YVO_4: Eu^{3+}, which proved the feasibility of EPR for the detection of crystal defects.[55] The calculated result in this study also indicate that the crystal defects were detected easily with an increase in temperature. Alternatively, the crystal defects in β-$NaYF_4$: 0.065Eu^{3+}, 0.002Sm^{3+} could capture electrons at room temperature steadily. To calculate the depth and density of defects, thermoluminescence spectra (TL spectra) were utilized, as shown in Fig. 10d. The following was employed:

$$E = T_m/500$$

$$N_0 = \omega \times I_m/\beta \times [2.52 + 10.2(\mu_g - 0.42)] \tag{10}$$

where E represents the trap depth. T_m (K) corresponds to the highest temperature of the TL spectra. N_0 is the densities of traps. I_m and β represent the TL peak intensity and heating rate (1 °C min^{-1}), respectively. Furthermore, ω represents $\tau + \delta$, where τ and δ are the low temperature half-width and high temperature half-width, respectively. In this study, δ is 271.365. The τ is zero, resulting from the absence of an obvious peak at low temperature. Finally, the μ_g parameter refers to $\delta/(\tau + \delta)$. According to eqn (9) and eqn (10),[56] the depth and densities of the traps are 1.11 eV and 3.4431 × 10^3, respectively.

The replacement between Na^+ and a lanthanide ion was reported,[47] where Eu^{2+} occupies the chemical position of Na^+. Thus, combining the single-type signal of EPR, eqn (7) and (8) can be modified to the following expression:

$$Na^+ + Y^{3+} \rightarrow V''_Y + V^{\cdot\cdot}_Y \tag{11}$$

Noticeably, the Eu element possesses two *g* values, which are equal to 0.6134 and 1.3887.[57] Similarly, the typical *g* values of the Sm element are −0.232 and 0.1908.[57] As shown in Fig. 10c, evident peaks were absent at the *g* value positions of 0.1908, 0.6134, and 1.3887, indicating that there were no unpaired electrons of Eu^{3+} and Sm^{3+} existing in the sample. Combining this result with Fig. 10b and c, the detected signal and calculated *g* value were confirmed to be crystal defects. This verified

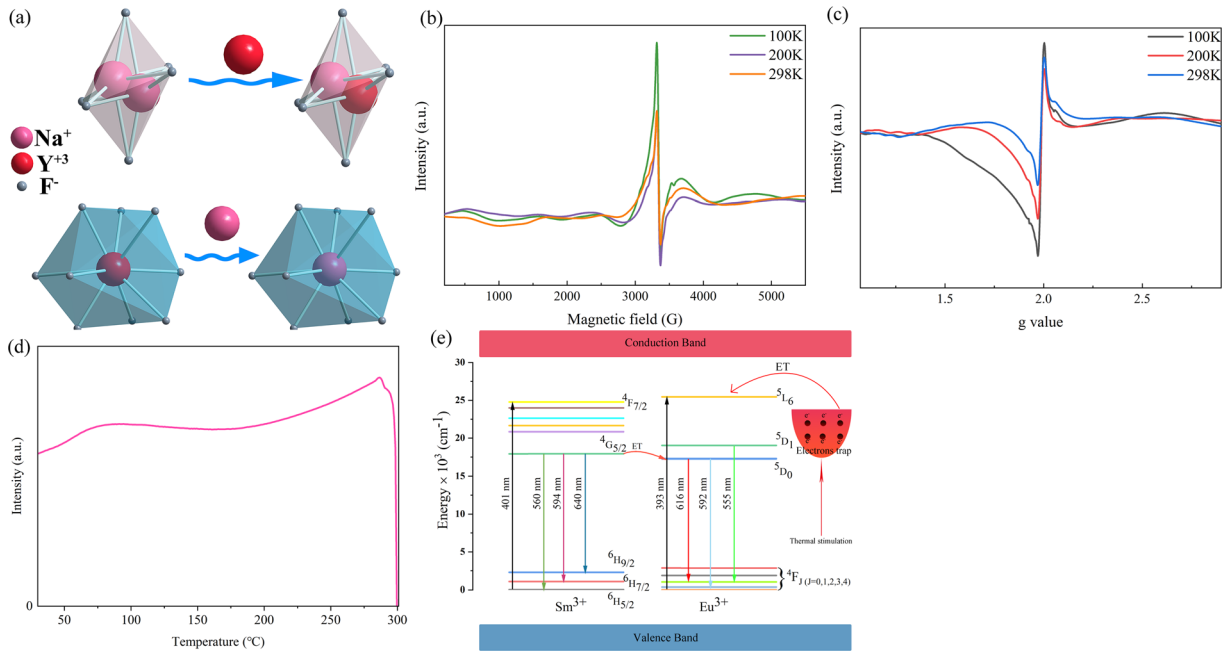

Fig. 10 (a) Replacement between Na^+ and Y^{3+}. (b) EPR spectra at 100 K, 200 K and 298 K. (c) Calculated g value based on EPR spectra. (d) TL spectra of $NaYF_4$: 0.065Eu^{3+}, 0.002Sm^{3+}. (e) Negative thermal quenching mechanism schematic diagram of $NaYF_4$: 0.065Eu^{3+}, 0.002Sm^{3+}.

that the V_Y'' and $V_Y^{\cdot}$ vacancies lead to NTQ for the $NaYF_4$: $0.065Eu^{3+}$, $0.002Sm^{3+}$ phosphor.

The NTQ mechanism diagram is presented in Fig. 10d. With an increase of temperature, the thermal active energy would be boosted simultaneously. Under the activity of mounting thermal active energy, the electrons stored inside the electronic traps would be released and excited to the $^5L_6$ energy level. Besides the interior electrons of Eu^{3+}, the electrons from the traps will be excited to the excited state and transit to the ground state as a counterpart to offset the decrease of luminous intensity induced by the non-radiative transition. In the temperature range of 303 K to 483 K, the luminous intensity increased, corresponding to the augmented number of excited electrons with an increase in the thermal energy. The NTQ performance can be concluded as the process of energy transfer from the thermal energy to electrons in traps. After heating to 483 K, the integrated luminous intensity showed a decline from 483 K to 543 K, which is attributed to the decrease in the number of released and excited electrons, as well as the normal thermal quenching. Besides, due to the decrease in the number of electrons inside the traps, the non-radiative transition effect will overpower the NTQ effect produced by the excited electrons stored in the traps, leading to a decrease in luminous intensity.

3.5 Fabrication of prototype red LEDs

The luminescent property of prototype red LED and luminous graph are illustrated in Fig. 11a. The prototype LED (LED (i)) was fabricated by coating the $NaYF_4$: $0.065Eu^{3+}$, $0.002Sm^{3+}$ sample on the surface of a 395 nm UV chip. The red-light portion could

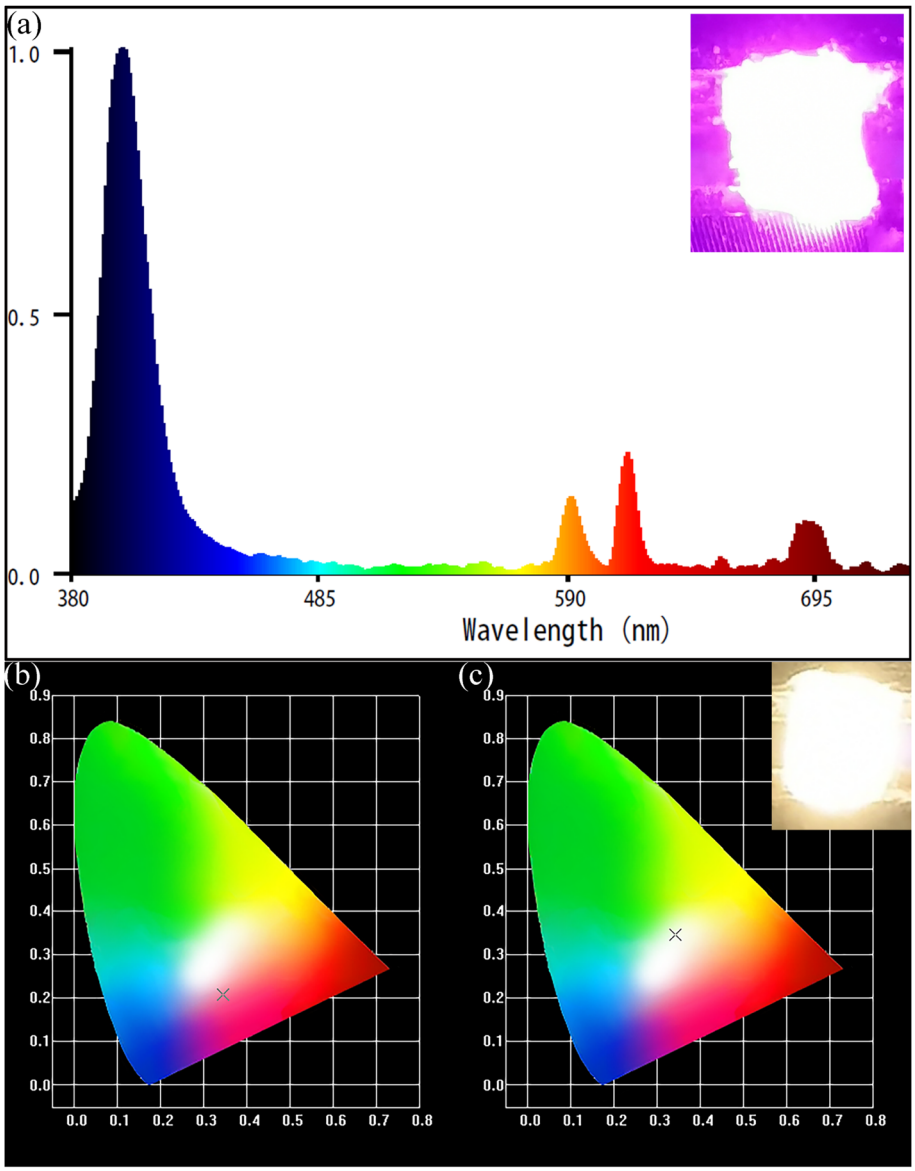

Fig. 11 (a) Luminescent performance of prototype LEDs ($NaYF_4$: $0.065Eu^{3+}$, $0.002Sm^{3+}$ + 395 nm UV chip) and luminescent graph. (b) CIE chromaticity diagram of fabricated LEDs. (c) CIE coordinate and fabricated WLEDs combining YAG: Ce^{3+} yellow phosphor with $NaYF_4$: $0.065Eu^{3+}$, $0.002Sm^{3+}$ phosphor and 395 nm UV chip.

reach 34.2% under the driving current of 10 mA. Fig. 11b depicts the CIE chromaticity diagram of LED(i), indicating it is close to the white light region. This result proves that the novel β-$NaYF_4$: $0.065Eu^{3+}$, $0.002Sm^{3+}$ has enormous potential as the red-light component of WLEDs. The prototype white light LED (LED (ii)) was fabricated by coating a mixture of $NaYF_4$: $0.065Eu^{3+}$, $0.002Sm^{3+}$ and YAG: Ce^{3+} on the surface of a 395 nm UV chip. Fig. 11c shows the CIE chromaticity diagram of LED (ii), indicating that it emits white light. The quantum efficiency and absorption efficiency of the sample reached 74.43% and 86.99%, respectively. The color temperature and color rendering index of LED (ii) were 5074 K and 81.6, respectively. Besides, the CIE coordinates of the prototype red LED is $(x, y) = (0.3461, 0.3387)$.

4. Conclusion

A series of $NaYF_4$: $0.065Eu^{3+}$, xSm^{3+} ($x = 0$–0.005) with dendritic crystal of high crystallinity was successfully synthesized *via* a one-step hydrothermal method. The effect of the luminous enhancement induced by energy transfer from Sm^{3+} to Eu^{3+} was observed. The energy transfer mechanism was explained to be the quadrupole–quadrupole interactions. When the concentration of Sm^{3+} was 0.001–0.005 mol%, the luminous intensities of $NaYF_4$: $0.065Eu^{3+}$, xSm^{3+} ($x = 0$, 0.001, 0.002, 0.003, 0.004, and 0.005 mol) were enhanced to 128.89%, 197.19%, 174.53%, 138.11%, and 139.69%, respectively, compared with the sample without co-doped Sm^{3+} ion. The energy transfer mechanism was explained by quadrupole–quadrupole interactions. Noteworthily, remarkable luminous thermal stability was found in the emission spectrum of $NaYF_4$: $0.065Eu^{3+}$, $0.002Sm^{3+}$. With an increase in temperature from 303 K to 483 K, the luminous intensity increased to 229.82% of that at 303 K. This is known as negative thermal quenching, and this outstanding thermal performance is attributed to the crystal point defects originating from the non-equivalence between Na^+ and Y^{3+} ions, which will lead to thermal stimulation excitement of the electrons captured in electronic traps.

Conflicts of interest

The authors declare that they have no known competing financial interests or personal relationships that could have appeared to influence the work reported in this paper.

Acknowledgements

This research is supported by the National Natural Science Foundation of China (Grant No. 21661006 and No. 21965004), the Natural Science Foundation of Guangxi Zhuang Autonomous Region, China (Grant No. 2019GXNSFDA245022, No. 2020GXNSFAA159036), the Scientific Research Foundation of Guangxi University (Grant No. XDZ140116), the innovation Project of Guangxi Graduate Education (Grant No. YCSW2020015), the Students Experimental Skills and Innovation Ability Training Fund Project of Guangxi University (No. 202010593186).

References

1 P. M. Pattison, J. Y. Tsao, G. C. Brainard and B. Bugbee, *Nature*, 2018, **563**, 493–500.
2 P. Pust, P. J. Schmidt and W. Schnick, *Nat. Mater.*, 2015, **14**, 454–458.
3 S. D. Carvalho and K. M. Folta, *Crit. Rev. Plant Sci.*, 2014, **33**, 486–508.
4 S. A. Rahman, M. A. St Hilaire and S. W. Lockley, *Physiol. Behav.*, 2017, **177**, 221–229.
5 T. Wu, C.-W. Sher, Y. Lin, C.-F. Lee, S. Liang, Y. Lu, S.-W. Huang Chen, W. Guo, H.-C. Kuo and Z. Chen, *Appl. Sci.*, 2018, **8**, 1557.
6 L. Xu, C. C. Ming, Y. Li, K. Fan, M. Zhang, H. Sun and Z. Guo, *IEEE Access*, 2021, **9**, 74713–74718.
7 D. Chen, Y. Zhou, W. Xu, J. Zhong, Z. Ji and W. Xiang, *J. Mater. Chem. C*, 2016, **4**, 1704–1712.
8 X. Huang, H. Guo and B. Li, *J. Alloys Compd.*, 2017, **720**, 29–38.
9 J. Ding, Q. Wu, Y. Li, Q. Long, Y. Wang and Y. Wang, *Chem. Eng. J.*, 2016, **302**, 466–474.
10 Z. Li, X. Zhang, J. Wu, R. Guo, L. Luo, Y. Xiong, L. Wang and W. Chen, *J. Mater. Chem. C*, 2021, **9**, 13236–13246.
11 M. L. Meretska, G. Vissenberg, A. Lagendijk, W. L. Ijzerman and W. L. Vos, *ACS Photonics*, 2019, **6**, 3070–3075.
12 D. Zhang, X. Zhang, Z. An, R. Dong, Z. Shi, Y. Song and H. Zou, *Inorg. Chem.*, 2020, **59**, 14193–14206.
13 M. Zhao, H. Liao, M. S. Molokeev, Y. Zhou, Q. Zhang, Q. Liu and Z. Xia, *Light: Sci. Appl.*, 2019, **8**, 38.
14 J. Ueda, P. Dorenbos, A. J. J. Bos, A. Meijerink and S. Tanabe, *J. Phys. Chem. C*, 2015, **119**, 25003–25008.
15 H. Daicho, T. Iwasaki, K. Enomoto, Y. Sasaki, Y. Maeno, Y. Shinomiya, S. Aoyagi, E. Nishibori, M. Sakata, H. Sawa, S. Matsuishi and H. Hosono, *Nat. Commun.*, 2012, **3**, 1132.
16 P. Pust, V. Weiler, C. Hecht, A. Tucks, A. S. Wochnik, A. K. Henss, D. Wiechert, C. Scheu, P. J. Schmidt and W. Schnick, *Nat. Mater.*, 2014, **13**, 891–896.
17 J. A. Kechele, C. Hecht, O. Oeckler, J. Schmedt auf der Günne, P. J. Schmidt and W. Schnick, *Chem. Mater.*, 2009, **21**, 1288–1295.
18 Q. Wei, J. Ding and Y. Wang, *Chem. Eng. J.*, 2020, **386**, 124004.
19 S. Yamada, H. Emoto, M. Ibukiyama and N. Hirosaki, *J. Eur. Ceram. Soc.*, 2012, **32**, 1355–1358.
20 S. Li, X. Zhang, Z. Hou, Z. Cheng, P. Ma and J. Lin, *Nanoscale*, 2012, **4**, 5619–5626.
21 R. Joshi, R. S. Perala, S. B. Shelar, A. Ballal, B. P. Singh and R. S. Ningthoujam, *ACS Appl. Mater. Interfaces*, 2021, **13**, 3481–3490.
22 M. F. Torresan and A. Wolosiuk, *ACS Appl. Bio Mater.*, 2021, **4**, 1191–1210.
23 E. Song, Y. Zhou, X.-B. Yang, Z. Liao, W. Zhao, T. Deng, L. Wang, Y. Ma, S. Ye and Q. Zhang, *ACS Photonics*, 2017, **4**, 2556–2565.
24 M. Calil Júnior, Á. Melo, E. Rodrigues, F. Sigoli and M. Rodrigues, *J. Braz. Chem. Soc.*, 2017, **28**, 1816–1821.

25 H. X. Mai, Y. W. Zhang, R. Si, Z. G. Yan, L. D. Sun, L. P. You and C. H. Yan, *J. Am. Chem. Soc.*, 2006, **128**, 6426–6436.
26 H. T. Phuong, T. T. Huong, L. T. Vinh, H. T. Khuyen, D. T. Thao, N. T. Huong, P. T. Lien and L. Q. Minh, *J. Rare Earths*, 2019, **37**, 1183–1187.
27 B. Dong, H. W. Song, H. Q. Yu, H. Zhang, R. F. Qin, X. Bai, G. H. Pan, S. Z. Lu, F. Wang, L. B. Fan and Q. L. Dai, *J. Phys. Chem. C*, 2008, **112**, 1435–1440.
28 J. Zhang and H. Riesen, *Chem. Phys. Lett.*, 2015, **641**, 1–4.
29 Y. Luo, R. Yang, X. Zhang, B. Hu, S. Hu, L. Zhou and J. Yang, *CrystEngComm*, 2015, **17**, 7762–7771.
30 K. Binnemans, *Coord. Chem. Rev.*, 2015, **295**, 1–45.
31 H.-Y. Lin, Y.-C. Fang and S.-Y. Chu, *J. Am. Ceram. Soc.*, 2010, **93**, 3850–3856.
32 Y. Huang, E. L. Hsiang, M. Y. Deng and S. T. Wu, *Light Sci. Appl.*, 2020, **9**, 105.
33 F. Mercier, C. Alliot, L. Bion, N. Thromat and P. Toulhoat, *J. Electron Spectrosc. Relat. Phenom.*, 2006, **150**, 21–26.
34 M. G. Brik, A. M. Srivastava and A. I. Popov, *Opt. Mater.*, 2022, **127**, 112276.
35 B. R. Judd, *Phys. Rev.*, 1962, **127**, 750–761.
36 G. S. Ofelt, *J. Phys. Chem.*, 1962, **37**, 511–520.
37 J. Zhang, G. Cai, W. Wang, L. Ma, X. Wang and Z. Jin, *Inorg. Chem.*, 2020, **59**, 2241–2247.
38 S. Fang, T. Lang, T. Han, J. Wang, J. Yang, S. Cao, L. Peng, B. Liu, A. N. Yakovlev and V. I. Korepanov, *Chem. Eng. J.*, 2020, **389**, 124297.
39 K. Li, J. Fan, M. Shang, H. Lian and J. Lin, *J. Mater. Chem. C*, 2015, **3**, 9989–9998.
40 C. Cao, H. K. Yang, J. W. Chung, B. K. Moon, B. C. Choi, J. H. Jeong and K. H. Kim, *J. Mater. Chem.*, 2011, **21**, 10342–10347.
41 B. Su, H. Xie, Y. Tan, Y. Zhao, Q. Yang and S. Zhang, *J. Lumin.*, 2018, **204**, 457–463.
42 Y. Liu, Y. Li, J. Meng, W. Liang, W. Huang, S. Liao, Y. Huang and H. Zhang, *J. Lumin.*, 2020, **217**, 116770.
43 Y. Liu, G. Zhang, J. Huang, X. Tao, G. Li and G. Cai, *Inorg. Chem.*, 2021, **60**, 2279–2293.
44 Y. Liu, R. Wang, Q. Yang, G. Li, J. Huang and G. Cai, *J. Am. Ceram. Soc.*, 2022, **105**, 6184–6195.
45 H. Ming, Y. Zhao, Y. Zhou, S. Zhang, Y. Wang, E. Song, Z. Xia and Q. Zhang, *ACS Appl. Electron. Mater.*, 2020, **2**, 4134–4145.
46 R. Shi, L. Ning, Z. Wang, J. Chen, T. K. Sham, Y. Huang, Z. Qi, C. Li, Q. Tang and H. Liang, *Adv. Opt. Mater.*, 2019, **7**, 1901187.
47 X. Wang, Z. Zhao, Q. Wu, C. Wang, Q. Wang, L. Yanyan and Y. Wang, *J. Mater. Chem. C*, 2016, **4**, 8795–8801.
48 G. Zhu, Z. Li, C. Wang, X. Wang, F. Zhou, M. Gao, S. Xin and Y. Wang, *Dalton Trans.*, 2019, **48**, 1624–1632.
49 V. I. Nefedov, Y. V. Salyn, G. Leonhardt and R. Scheibe, *J. Electron Spectrosc. Relat. Phenom.*, 1977, **10**, 121–124.
50 H. Seyama, *J. Chem. Soc., Faraday Trans. 1*, 1985, **81**, 485–495.
51 R. P. Vasquez, M. C. Foote and B. D. Hunt, *J. Appl. Phys.*, 1989, **66**, 4866–4877.
52 U. Yoshinori, T. Akira, I. Toshio and Y. Hideo, *Bull. Chem. Soc. Jpn.*, 1986, **59**, 2263–2267.
53 K. Ye, K. Li, Y. Lu, Z. Guo, N. Ni, H. Liu, Y. Huang, H. Ji and P. Wang, *TrAC, Trends Anal. Chem.*, 2019, **116**, 102–108.
54 F. Tang, Z. Su, H. Ye, W. Gao, X. Pan and S. Xu, *ACS Omega*, 2018, **3**, 13704–13710.
55 L. Yang, S. Peng, M. Zhao and L. Yu, *Appl. Surf. Sci.*, 2019, **473**, 885–892.
56 K. Van den Eeckhout, P. F. Smet and D. Poelman, *Materials*, 2010, **3**, 2536–2566.
57 J. R. B and J. A. Weil, *Electron Paramagnetic Resonance: Elementary Theory Electron and Practical applications*, 2nd, John Wiley & Sons, Hoboken, 2007.